Deep learning–based enhancement of feature tracking for sea ice drift estimation

Ki-Yeong Mun[1], Junhwa Chi[1,*]

[1]Division of Data Information Sciences, Pukyong National University, Busan, Republic of Korea
- mansrl0929@pukyong.ac.kr, jchi@pknu.ac.kr

Commission III, WG III/7

Keywords: Sea Ice Drift, Feature Tracking, Synthetic Aperture Radar, Computer Vision, Deep Learning

Abstract

Sea Ice Drift (SID) is an important parameter in understanding the Arctic climate dynamics and in maintaining navigation safety for the Arctic waters. SID is typically derived from keypoints extracted and matched from Synthetic Aperture Radar (SAR) imagery and is represented as a grid-based field. However, in feature tracking, the widely used Oriented FAST and Rotated BRIEF (ORB) is inherently vulnerable to low contrast, speckle noise, and complex sea ice deformation in feature tracking. To address these limitations, we propose an SID estimation framework that replaces the conventional ORB with deep learning-based methods such as SuperGlue and Local Feature TRansformer (LoFTR). In addition, multi-polarization is applied to exploit complementary information across both the feature tracking and pattern matching stages. Under polarization integration, SuperGlue reduced speed and directional RMSE by 50.8% and 37.3%, respectively, compared to ORB, while LoFTR achieved the best performance with reductions of 70.0% and 41.0%. These results demonstrate that deep learning-based methods can effectively replace the conventional ORB approach for SID estimation in the Arctic environments.

1. INTRODUCTION

Sea ice, formed by the freezing of seawater in polar regions, is a critical indicator of global ocean circulation and polar ecosystems. It is a constant state of motion, driven by wind and ocean currents; this external forcing leads to convergence and divergence, causing the ice to fracture or collide (Liang et al., 2024). These processes result in various structural features, such as leads and ridges, which significantly alter the physical structure and distribution of the ice cover. In recent years, the surface area and thickness of Arctic sea ice have been declining rapidly due to the effects of global warming (Kwok, 2018), leading to a marked increase in ice mobility and variability. Observational data from 1992 to 2009 indicate that the average drift speed of Arctic sea ice has increased by approximately 10.6±0.9% per decade (Spreen et al., 2011). Such abrupt fluctuations in Sea Ice Drift (SID) pose significant challenges, including reduced navigational safety, increased collision risk, and uncertainty in predicting ice behavior. Conversely, the reduction in sea ice presents new opportunities for the development of Northern Sea Routes (Liu et al., 2024). While declining sea ice may extend navigable periods and provide economic benefits, such as shorter shipping routes, these advantages require accurate predictions of localized sea ice deformation and drift.

Early SID observations relied on in situ measurements, where buoys deployed on sea ice were used to track drift speed and direction (Rabault et al., 2023). However, these methods are limited by sparse spatial coverage, difficulty in long-term data collection (Giles et al., 2011), and high labor requirements. Recently, satellite-based SID observations have become more prevalent, with prominent methods utilizing Passive Microwave (PMW) and Synthetic Aperture Radar (SAR) data.

While PMW-based SID observations offer the advantage of continuous monitoring across the entire Arctic region, their coarse spatial resolution (25–75 km) limits their capacity to analyze localized sea ice deformation or detailed drift characteristics (Shi et al., 2024). In contrast, SAR-based SID observations provide high spatial resolution (on the order of several kilometers), enabling a more granular analysis of SID (Park et al., 2021). However, due to satellite orbital characteristics, SAR is constrained by limited revisit cycles and observation frequencies, making simultaneous wide-area coverage difficult (Kwok, 2017). In essence, each SID observation involves a trade-off between spatial and temporal resolution. This study focuses on a SAR-based retrieval method, which is advantageous for detecting localized sea ice deformation and leads—both of which are critical for maritime navigation.

SAR-based SID estimation typically begins with feature tracking between SAR image pairs, followed by Maximum Cross-Correlation (MCC)-based template matching to derive grid-based SID (Muckenhuber et al., 2016; Park et al., 2023; Wang et al., 2023; Lu et al., 2024). In this workflow, the speed and direction calculated through optimal template matching constitute the final SID. The quality of the final SID depends heavily on accurate feature matching in the preceding stage. Currently, the feature tracking stage for SID estimation is primarily performed using traditional computer vision methods. However, these methods struggle to maintain stable matching performance, as they are highly sensitive to intensity variations between images, speckle noise, and complex sea ice deformations. Consequently, there is a growing need for deep learning-based methods to achieve robust and accurate correspondence detection.

With recent advancements in deep learning technology, learning-based feature detection and matching algorithms based on Convolutional Neural Networks (CNNs) have evolved rapidly. This approach moves beyond traditional sparse methods based on interest point detection and leverages both global and local contextual information. Such a framework enables stable dense matching even in scenarios involving abrupt sea ice deformation, where computer vision methods often fail. Consequently, this suggests that more reliable SID estimation can be achieved within complex polar environments.

We aim to achieve high-precision SID estimation that can handle increasingly dynamic polar environments. To this end, a large-scale dataset covering the entire Arctic was constructed, including key regions with diverse sea ice conditions. While the methodology is built upon a widely utilized commercial SID estimation algorithm (Korosov and Rampal, 2017), the feature

* Corresponding author

tracking stage has been replaced with a deep learning-based method. Furthermore, the overall estimation performance was enhanced by refining the specific algorithmic procedures and incorporating multi-polarization information. Through these advancements, this research seeks to provide more stable and reliable SID observations in a polar environment marked by climate-driven variability, ultimately improving sea ice monitoring and navigation safety along Northern Sea Routes.

2. DATASET

2.1 Buoy Data

For quantitative evaluation of SID, we used observational data from Ice-Tethered Profiler (ITP) buoys. Deployed directly on Arctic sea ice, ITP buoys drift with the ice cover and provide long-term observations of oceanographic parameters such as temperature and salinity. They are widely used in Arctic oceanography and sea ice research (Toole et al., 2015). Because changes in buoy position directly reflect ice drift, these data serve as reliable ground-truth references for SID validation.
The buoy data analyzed in this study were collected from January to December 2024. To capture diverse ice conditions, the buoys cover major Arctic regions with distinct sea ice characteristics. The study area includes the Chukchi and East Siberian Seas, where sea ice decline and summer melt have intensified in recent decades. It also includes the Beaufort Sea, which shows high variability in ice thickness and distribution due to a mix of multi-year and first-year ice. In addition, the Central Arctic Ocean is included, where multi-year ice remains relatively stable year-round (Kwok et al., 2013; Meier and Stroeve, 2022). This regional configuration captures trends in sea ice decline, seasonal variability, and drift dynamics, enabling robust evaluation across diverse cryospheric environments.

2.2 Sentinel-1 SAR Data

To estimate SID, we used Google Earth Engine (GEE) to construct an image pair dataset. GEE is a cloud-based platform designed for planetary-scale geospatial analysis, offering a vast catalog of publicly available geospatial data. A key advantage of this platform is its ability to efficiently process both long-term archived and near-real-time data using parallel computing (Gorelick et al., 2018).
Sentinel-1 SAR imagery, which provides consistent coverage across the Arctic, was selected for this study. Data acquisition was synchronized with buoy observations, and each image was centered on the buoy position. This approach allows buoy data to be directly integrated into image pairs, enabling reliable validation of SID estimates. In addition, both HH and HV polarization channels were utilized. HV polarization is sensitive to surface roughness and structural changes, whereas HH polarization captures sea ice characteristics based on surface scattering (Segal et al., 2020; Jin et al., 2026). Combining these polarizations provides more comprehensive feature information.
SAR imagery requires preprocessing, including conversion of Digital Number (DN) values into intensity values for physical interpretation. Accordingly, raw DN values were converted into the backscattering coefficient (σ^0). For Sentinel-1 SAR imagery, σ^0 is defined as follows:

$$\sigma^0 = 10 \cdot \log(\mathrm{DN}^2) \tag{1}$$

σ^0 is normalized using min–max scaling and converted into 8-bit integer data (σ_8^0), ranging from 0 to 255. This conversion process is defined as follows:

$$\sigma_8^0 = 255 \cdot \frac{\sigma^0 - \sigma_{\min}^0}{\sigma_{\max}^0 - \sigma_{\min}^0} \tag{2}$$

where $\sigma_{\max}^0$ = maximum value of σ^0 for each polarization
$\sigma_{\min}^0$ = minimum value of σ^0 for each polarization

All images are of size 1000 × 1000 pixels. Spatial resolution was reduced by downsampling, averaging adjacent pixels to suppress speckle noise, resulting in a final pixel size of 80 × 80 m. The data were organized into image pairs with temporal intervals of 1–6 days, and only pairs with more than 50% spatial overlap were retained.
In total, 398 image pairs were constructed. Figure 1 visualizes the spatial distribution and density of the constructed dataset by aggregating the data into 25 km grid cells.

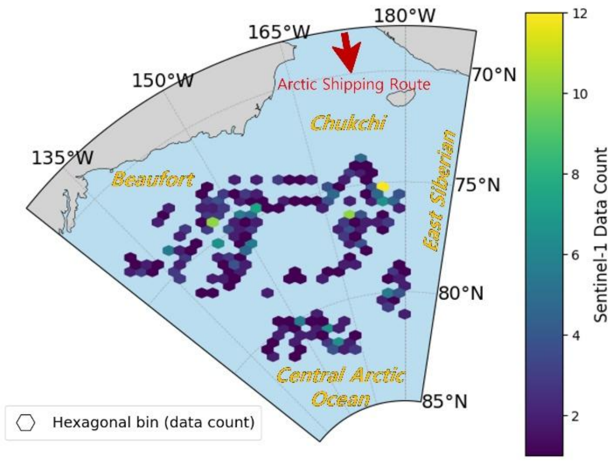

Figure 1. Spatial distribution of the dataset over the Arctic Ocean.

Figure 2 illustrates the monthly distribution of the constructed dataset, clearly highlighting seasonal variations in data composition. In particular, the summer months exhibit a decreasing trend in the number of available image pairs. This is primarily due to the active melting and rapid deformation of sea ice, which leads to increased drift speeds; consequently, the overlapping area between consecutive images is reduced, hindering the successful generation of viable image pairs.

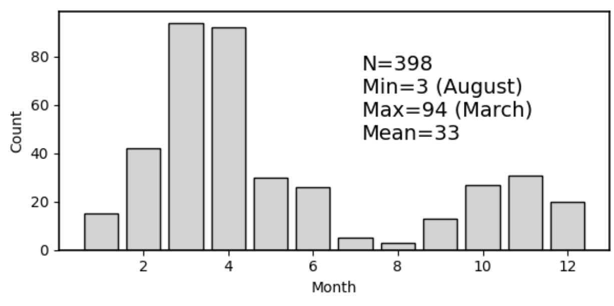

Figure 2. Monthly distribution of the dataset.

Figure 3 presents examples of the image pairs. In both images, T_1 and T_2, a buoy is positioned at the center, and its displacement is observed over time. Based on the buoy’s trajectory, it is confirmed that the sea ice also drifts with a consistent directional trend, following the movement of the buoy.

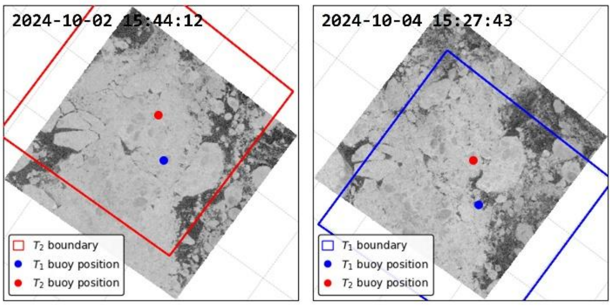

Figure 3. Example of a SAR image pair with the buoy at the center.

3. METHODS

This section details the architecture of the algorithm used for SID estimation. In particular, we focus on the core contribution of this study: the enhancement of estimation performance by replacing the feature tracking stage with a deep learning-based method. In addition, we describe how multi-polarization information is utilized in both the feature tracking and pattern matching stages.

3.1 SID Estimation

The baseline is an open-source SID estimation algorithm developed by the Nansen Environmental and Remote Sensing Center (NERSC). This algorithm derives SID from Sentinel-1 SAR imagery as a vector field. The overall workflow consists of three stages.

The first stage estimates the initial SID through feature tracking between image pairs acquired at different times. In this step, keypoints are extracted using the Oriented FAST and Rotated BRIEF (ORB), and corresponding pairs are established via brute-force matching. This process estimates pixel coordinates (x_1, y_1) in the first image and their corresponding coordinates (x_2, y_2) in the second image, generating initial SID vectors.

To improve reliability, an outlier removal step was applied. Physically unrealistic drift was removed using a threshold of 0.5 m/s. The SID speed (v) is defined as:

$$v = \frac{\|d\|}{\Delta t} \quad (3)$$

where $d = (x_2 - x_1, y_2 - y_1)$
Δt = time difference between the image pair

A least-squares-based filter is then applied to ensure spatial consistency. A polynomial model calculates the residual error (ϵ) between estimated and observed coordinates. Vectors with errors exceeding 200 pixels are removed. The error is defined as follows:

$$\epsilon = \sqrt{(x_2 - \hat{x}_2)^2 + (y_2 - \hat{y}_2)^2} \quad (4)$$

where (x_2, y_2) = observed coordinates in the second image
$(\hat{x}_2, \hat{y}_2)$ = model-estimated coordinates

This process suppresses noise and spurious matches, resulting in reliable initial SID vectors.

The second stage generates a spatially continuous drift field from the sparse feature tracking vectors. To achieve this, a grid-based field is constructed over the entire image domain. Each grid cell is assigned a displacement based on initial SID vectors, and empty cells are filled by linear interpolation. This preliminary drift field, referred to as "First Guess", constrains the search range and improves computational stability during pattern matching.

The third stage performs MCC-based pattern matching to finalize SID vectors. At each grid point, the search area is defined using the preliminary drift vector. Correspondence is then determined through rotation-aware template matching. The location and rotation with the highest MCC value are selected as the optimal match. Consequently, this process generates a spatially continuous and physically consistent SID vector field.

The accuracy of this final SID field depends on high-quality feature pairs from the feature tracking stage, which estimates the initial SID (Li et al., 2022; Fang et al., 2023). However, ORB-based feature tracking often suffers from low feature density, particularly in low-texture regions or areas experiencing abrupt sea ice deformation (Demchev et al., 2017). Furthermore, brute-force matching incurs high computational cost, which limits efficiency during large-scale data processing (Jakubovic and Velagic, 2018). To overcome these constraints, we propose replacing conventional ORB-based feature tracking with deep learning-based methods. This enables denser and more stable correspondences, improving SID estimation in complex sea ice conditions.

Furthermore, to overcome the limitations of single-polarization, both HH and HV polarization channels were utilized simultaneously. Incorporating multi-polarization allows for the acquisition of richer SID data compared to using either polarization independently (Zhang et al., 2020). Accordingly, in the feature tracking stage, keypoint extraction and matching are performed separately for the HH and HV polarized images; the results from both channels are then integrated to generate a more stable set of initial SID vectors. Going a step further, the pattern matching stage also involves performing MCC-based matching for each polarization independently. The final vector is then determined by selecting the result with the higher correlation coefficient, thereby enhancing the reliability of the output. Incorporating multi-polarization provides matching robustness, particularly in low-texture regions and areas with significant sea ice deformation, leading to more accurate SID estimation. Figure 4 illustrates the overall workflow of the proposed SID estimation framework.

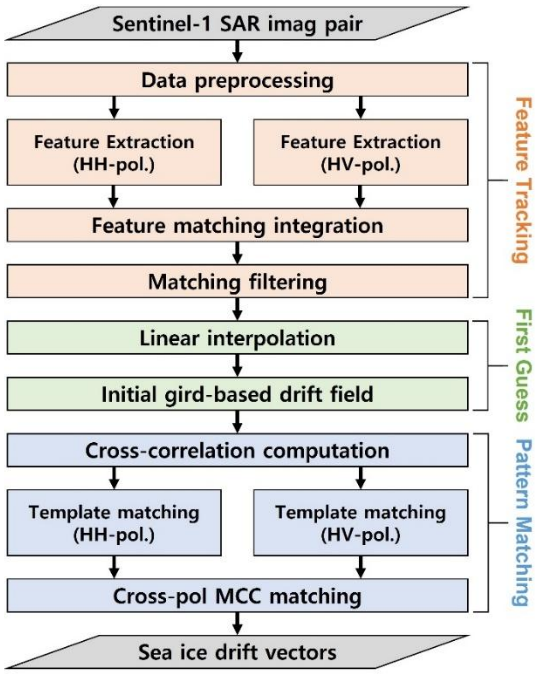

Figure 4. Overall workflow of the proposed SID estimation framework.

3.2 Deep learning-based Feature Tracking

Recent advances in deep learning have led to two main approaches in feature matching. Traditional approaches relied on CNN-based architectures to extract features and detect keypoints, followed by learned matching. Recently, attention has shifted toward detector-free methods that estimate correspondences directly from full feature maps, bypassing explicit keypoint detection. We adopted SuperGlue and Local Feature TRansformer (LoFTR) as representative methods for these two approaches.

3.2.1 SuperGlue: SuperGlue (Sarlin et al., 2020) is an algorithm that combines Graph Neural Networks (GNNs) and Transformer-based attention to model intra- and inter-image relationships. It takes keypoints and descriptors extracted from a conventional detector (e.g., SuperPoint) as input. Self- and cross-attention layers refine feature representations by modeling intra- and inter-image relationships. The refined features are used to compute a similarity matrix for correspondence estimation. Final matches are obtained by selecting correspondences with the highest similarity scores. While this strategy effectively captures complex spatial and contextual correlations during the matching process, this approach has limitations. Because it relies on descriptor-based matching, it struggles to establish stable correspondences in low-texture or repetitive regions.

3.2.2 LoFTR: LoFTR (Sun et al., 2021) is a detector-free method that directly estimates correspondences using a Transformer-based architecture, without explicit keypoint detection or descriptor generation. It uses multi-scale feature maps extracted by a ResNet-FPN backbone. Self- and cross-attention are applied to learn relationships from low-resolution feature maps. An initial set of correspondences is generated in a coarse matching stage. These correspondences are refined using a coarse-to-fine refinement process with high-resolution feature maps for precise localization. This enables both global context and local precision, allowing dense matching even in homogeneous sea ice regions.

3.3 Evaluation Metrics

To evaluate SID estimation performance, we compared ORB-based feature tracking with deep learning-based methods (SuperGlue and LoFTR) in terms of matching density and motion estimation accuracy. Feature extraction and matching capabilities were evaluated using the number of matched keypoints and estimated SID vectors. Drift speed and direction were evaluated using buoy data based on Root Mean Square Error (RMSE) and the coefficient of determination (R^2). RMSE and R^2 are defined as:

$$\mathrm{RMSE} = \sqrt{\frac{1}{\mathrm{N}}\sum_{i=1}^{N}\left\|\mathrm{v}_{\mathrm{i}}^{\mathrm{pred}} - \mathrm{v}_{\mathrm{i}}^{\mathrm{buoy}}\right\|^2} \tag{5}$$

$$\mathrm{R}^2 = 1 - \frac{\sum_{\mathrm{i}=1}^{\mathrm{N}}\left\|\mathrm{v}_{\mathrm{i}}^{\mathrm{pred}} - \mathrm{v}_{\mathrm{i}}^{\mathrm{buoy}}\right\|}{\sum_{\mathrm{i}=1}^{\mathrm{N}}\left\|\mathrm{v}_{\mathrm{i}}^{\mathrm{pred}} - \overline{\mathrm{v}}^{\mathrm{buoy}}\right\|} \tag{6}$$

where $\mathrm{v}_{\mathrm{i}}^{\mathrm{pred}}$ = predicted SID vector at sample i
$\mathrm{v}_{\mathrm{i}}^{\mathrm{buoy}}$ = buoy-derived SID vector at sample i
$\overline{\mathrm{v}}^{\mathrm{buoy}}$ = mean of buoy-derived SID vectors
N = number of samples

In addition, qualitative evaluation of the final drift vectors was performed.

3.4 Experimental Setup

All experiments were conducted on a Windows 11 system with an Intel Core i9-12900K CPU, an NVIDIA RTX 4090 GPU, and 128 GB RAM. The deep learning-based models were pre-trained on ScanNet and MegaDepth, and outdoor-trained weights were used.
To improve matching precision, confidence-based filtering was applied. For ORB, Lowe's ratio test with a similarity threshold of 0.75 was applied. For deep learning-based methods, only correspondences with a confidence score ≥ 0.5 were retained. Additionally, matches with MCC ≥ 0.3 were retained. The final SID vector field was generated at 3 km resolution.

4. RESULTS AND DISCUSSION

4.1 Polarization Integration Effects on Feature Tracking

Keypoint sets were expanded by extracting correspondences independently from HH and HV polarized images and then integrating them. During integration, keypoints within 3 pixels were considered redundant, and only the one with higher confidence was retained. Otherwise, they were treated as distinct and merged into the final set. Table 1 summarizes the number of extracted keypoints and SID vectors for each polarization (HH, HV) and their integration (HH+HV).

Polarisation	Algorithm	Keypoint count	Vector count
HH	ORB	1260.719	1967.437
	SuperGlue	330.666	1962.477
	LoFTR	2737.470	1994.683
HV	ORB	1156.613	1947.224
	SuperGlue	273.497	1945.158
	LoFTR	2468.817	1976.304
HH+HV	ORB	1676.764	1982.651
	SuperGlue	376.961	1971.119
	LoFTR	2888.527	2008.596

Table 1. Performance comparison of feature tracking algorithms in terms of keypoint and vector counts.

Table 1 shows that all three algorithms extract more keypoints from HH than from HV polarization. This is consistent with previous studies (Lohse et al., 2021), which report that HV polarization has lower signal intensity and is more affected by speckle noise than HH. Thus, HV polarization is less effective than HH for extracting features related to dynamic SID.
Multi-polarization increases the number of keypoints across all algorithms. The increases were 33.0% for ORB, 14.0% for SuperGlue, and 5.5% for LoFTR. The smaller increase in deep learning-based methods is due to their ability to generate sufficient correspondences from a single polarization. The consistent increase indicates that HH and HV provide complementary features rather than redundant detections. This suggests that each polarization captures distinct backscattering and texture patterns, leading to expanded keypoint coverage.
Although vector counts also increased, the magnitude was smaller than that of keypoints. This is because the final SID vectors are generated on a grid. Once sufficient keypoints are available, vector generation quickly saturates at the grid level. Additional keypoints primarily improve stability within each grid cell rather than increasing the total number of vectors. The increase in the number of vectors is also attributed to polarization

integration during the pattern matching stage. Selecting the higher MCC result from each polarization increases the number of valid SID vectors (MCC ≥ 0.3).

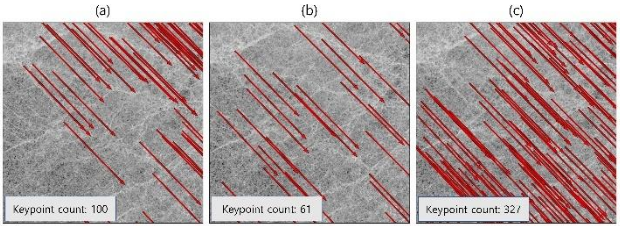

Figure 5. Initial SID vectors generated by each algorithm. (a) ORB, (b) SuperGlue, and (c) LoFTR.

Figure 5 presents initial SID vectors for a case with a consistent direction flow. ORB yields many keypoints, but they are locally clustered in high-response regions (e.g., corners and edges) within the image. Although SuperGlue produces fewer keypoints, they are more globally distributed, with points dispersed across a much wider area. This global distribution leads to the generation of more abundant and stable SID vectors, with SuperGlue achieving a comparable number of vectors despite having significantly fewer keypoints than ORB. This suggests that spatial distribution is more important than the absolute number of keypoints for SID estimation. Meanwhile, as shown in Figure 5, LoFTR generates the most keypoints with both local and global coverage. This demonstrates that LoFTR achieves both high correspondence density and broad spatial coverage, outperforming other methods.

4.2 SID Estimation Performance

This section evaluates the accuracy of the estimated SID vectors. Table 2 presents the speed and directional accuracy of SID vectors for each algorithm under single polarizations and their integration. Figure 6 shows scatter plots of SID vectors under polarization integration for all algorithms.

Polarisation	Algorithm	SID Speed		SID Direction	
		RMSE	R^2	RMSE	R^2
HH	ORB	1.048	0.968	12.923	0.895
	SuperGlue	0.492	0.993	6.532	0.931
	LoFTR	0.256	0.998	5.707	0.950
HV	ORB	1.546	0.930	18.130	0.903
	SuperGlue	0.625	0.988	10.322	0.935
	LoFTR	0.577	0.990	9.444	0.936
HH+HV	ORB	0.664	0.987	9.445	0.925
	SuperGlue	0.327	0.997	5.919	0.950
	LoFTR	0.199	0.999	5.577	0.951

Table 2. SID estimation performance under different polarization conditions.

Consistent with feature tracking results, Table 2 shows that HH polarization generally yields lower RMSE and higher R^2 than HV across all algorithms. This indicates that lower signal intensity and speckle noise in HV reduce accuracy in both speed and direction. However, it cannot be concluded that one polarization is inherently superior. Since HV can provide higher information content in certain conditions (Zhao et al., 2024), these results should be interpreted within our experimental context. Because each polarization contains unique information, integrating multi-polarization across both stages is more effective. Polarization integration consistently improves performance across all metrics. As demonstrated in Table 2, multi-polarization reduces RMSE and increases R^2 for both speed and direction across all algorithms. This demonstrates that integrating multi-polarization throughout the pipeline is highly effective.

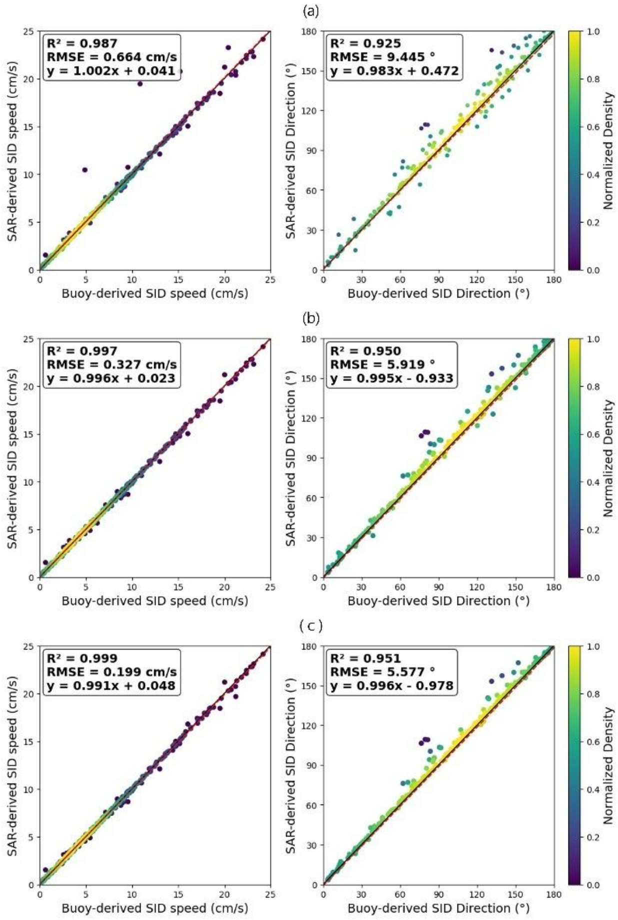

Figure 6. Scatter plots of buoy-derived vs. predicted SID vectors for each algorithm (HH+HV). (a) ORB, (b) SuperGlue, and (c) LoFTR.

Performance differences between algorithms are clearly observed. A consistent ranking was observed: LoFTR performs best, followed by SuperGlue, and then ORB. Compared to ORB, SuperGlue reduces speed RMSE by 50.8% and directional RMSE by 37.3%. LoFTR shows larger improvements, reducing speed RMSE by 70.0% and directional RMSE by 41.0%. These results demonstrate that deep learning-based methods significantly outperform traditional approaches. In particular, dense correspondence methods outperform approaches based on sparse keypoints in SID estimation.

4.3 Temporal Performance Comparison

Arctic sea ice density varies significantly with season. To analyze temporal error variations, Figure 7 illustrates monthly RMSE for speed and direction from January to December as a heatmap. Errors increase during summer across all algorithms for both speed and direction. This is attributed to surface melting, which forms melt ponds and reduces backscattering (Scharien et al., 2010). However, SuperGlue and LoFTR consistently show lower errors than ORB across all months, including summer. These results demonstrate that deep learning-based methods maintain superior performance across seasonal variations and remain robust under rapidly changing conditions.

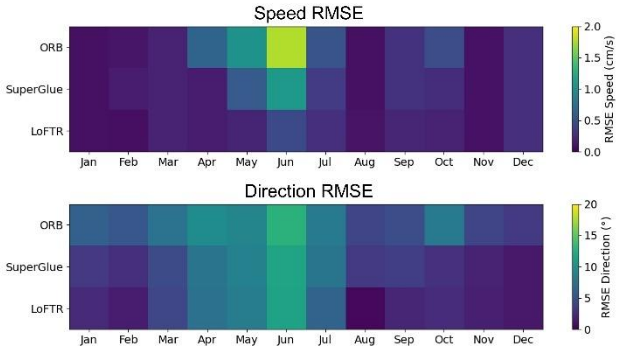

Figure 7. Monthly RMSE (speed and direction) for each algorithm (HH+HV).

4.4 Qualitative Analysis of SID Vector Field

This section provides a qualitative evaluation of the SID vector field. Figure 8 presents Case 1, with consistent directional flow, while Figure 9 illustrates Case 2, with divergent flow and localized deformation. In both cases, ORB is compared with LoFTR, which showed the best quantitative performance.

In Case 1, where sea ice moves in a consistent direction with large displacement, ORB fails to generate a uniform SID vector field in regions with sparse initial vectors. In contrast, LoFTR generates a stable and coherent SID vector field that accurately captures overall ice motion.

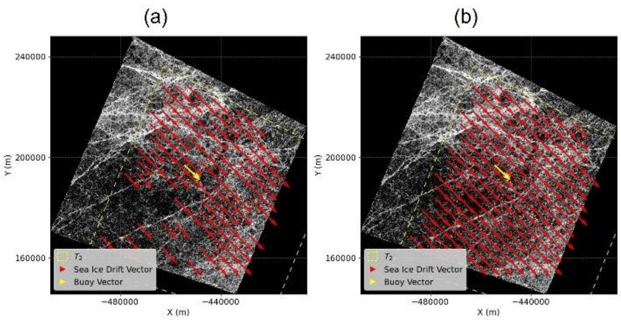

Figure 8. SID vector fields for Case 1 (consistent directional flow). (a) ORB and (b) LoFTR.

Case 2 is more challenging, with small overall displacement and strong localized deformations. In this case, ORB produces sparse vectors with unstable directions, reducing overall reliability. In contrast, LoFTR produces accurate and consistent SID vectors even under complex deformation. These results indicate that dense matching enables reliable SID estimation even in complex deformation scenarios.

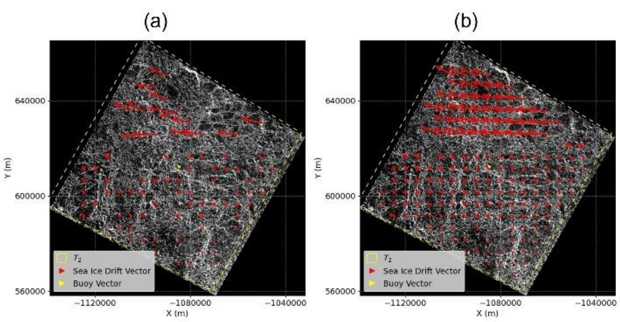

Figure 9. SID vector fields for Case 2 (divergent flow with local deformation). (a) ORB and (b) LoFTR.

5. CONCLUSION

This study applied deep learning-based feature tracking algorithms to estimate SID from Sentinel-1 SAR imagery. The baseline ORB was replaced with SuperGlue and LoFTR, enabling more robust and efficient matching through learning-based representations and global context. Furthermore, to effectively utilize multi-polarization information, a multi-polarization strategy was applied across both feature tracking and pattern matching stages.

Experimental results show that polarization integration reduces speed and directional RMSE while increasing R^2. Under the polarization integration condition, performance followed a clear hierarchy: LoFTR performed best, followed by SuperGlue and ORB. In this setting, SuperGlue reduced speed RMSE by 50.8% and directional RMSE by 37.3% compared to ORB. LoFTR achieved the best performance, reducing speed and directional RMSE by 70.0% and 41.0%, respectively. Furthermore, performance improvements were also observed during the rapidly changing Arctic summer conditions, and qualitative evaluation confirmed the generation of dense and coherent SID vector fields. Overall, deep learning-based methods significantly improve SID estimation performance, enabling stable and highly reliable results in the Arctic environment characterized by sea ice reduction, seasonal variability, and dynamic drift patterns.

However, this study has several limitations. As the analysis is based on data from a single year (2024) and is constrained by the limited availability of summer observations, it is difficult to fully generalize the performance of all algorithms. Furthermore, since the deep learning-based methods were applied using pre-trained weights, they are not specifically optimized for SAR imagery.

In future research, a large-scale SAR sea ice dataset will be constructed over extended periods by establishing an automated data collection framework using GEE. Furthermore, matching accuracy can be further improved through fine-tuning that reflects SAR-specific characteristics.

Acknowledgements

This work was supported by Korea Polar Research Institute (KOPRI) grant funded by the Ministry of Oceans and Fisheries (KOPRI PE26911).

References

Demchev, D., Volkov, V., Kazakov, E., Alcantarilla, P.F., Sandven, S., Khmeleva, V., 2017. Sea ice drift tracking from sequential SAR images using accelerated-KAZE features. IEEE Trans. Geosci. Remote Sens., 55(9), 5177–5191. doi.org/10.1109/TGRS.2017.2705678.

Fang, Y., Wang, X., Li, G., Chen, Z., Hui, F., Cheng, X., 2023. Arctic sea ice drift fields extraction based on feature tracking to MODIS imagery. Int. J. Appl. Earth Obs. Geoinf., 120, 103353. doi.org/10.1016/j.jag.2023.103353.

Giles, A.B., Massom, R.A., Heil, P., Hyland, G., 2011. Semi-automated feature-tracking of East Antarctic sea ice from Envisat ASAR imagery. Remote Sens. Environ., 115(9), 2267–2276. doi.org/10.1016/j.rse.2011.04.027.

Gorelick, N., Hancher, M., Dixon, M., Ilyushchenko, S., Thau, D., Moore, R., 2017. Google Earth Engine: Planetary-scale geospatial analysis for everyone. Remote Sens. Environ., 202, 18–27. doi.org/10.1016/j.rse.2017.06.031.

Jakubovic, A., Velagic, J., 2018. Image feature matching and object detection using brute-force matchers. Proc. 2018 Int. Symp. ELMAR, 83–86. doi.org/10.23919/ELMAR.2018.8534641.

Jin, F., Zhang, W., Yin, X., Zhang, J., Chu, Q., Li, G., Hu, S., 2026. Sea ice classification with GaoFen-3 fully polarimetric SAR and Landsat optical data. Remote Sens., 18(1), 74. doi.org/10.3390/rs18010074.

Korosov, A., Rampal, P., 2017. A combination of feature tracking and pattern matching with optimal parametrization for sea ice drift retrieval from SAR data. Remote Sens., 9(3), 258. doi.org/10.3390/rs9030258.

Kwok, R., 2017. Satellite remote sensing of sea-ice thickness and kinematics: a review. J. Glaciol., 56(200), 1129–1140. doi.org/10.3189/002214311796406167.

Kwok, R., 2018. Arctic sea ice thickness, volume, and multiyear ice coverage: losses and coupled variability (1958–2018). Environ. Res. Lett., 13(10), 105005. doi.org/10.1088/1748-9326/aae3ec.

Kwok, R., Spreen, G., Pang, S., 2013. Arctic sea ice circulation and drift speed: Decadal trends and ocean currents. J. Geophys. Res. Oceans, 118(5), 2408–2425. doi.org/10.1002/jgrc.20191.

Li, M., Zhou, C., Chen, X., Liu, Y., Li, B., Liu, T., 2022. Improvement of the feature tracking and pattern matching algorithm for sea ice motion retrieval from SAR and optical imagery. Int. J. Appl. Earth Obs. Geoinf., 112, 102908. doi.org/10.1016/j.jag.2022.102908.

Liang, X., Bi, H., Liu, C., Li, X., Wang, D., Zhao, F., Tian, Z., Li, M., Liu, N., 2024. The linkage between wintertime sea ice drift and atmospheric circulation in an Arctic ice–ocean coupled simulation. Ocean Modelling, 189, 102362. doi.org/10.1016/j.ocemod.2024.102362.

Liu, Y., Luo, H., Min, C., Chen, Q., Yang, Q., 2024. Changes in the Arctic Traffic Occupancy and Their Connection to Sea Ice Conditions from 2015 to 2020. Remote Sens., 16(7), 1157. doi.org/10.3390/rs16071157.

Lohse, J., Doulgeris, A.P., Dierking, W., 2021. Incident angle dependence of Sentinel-1 texture features for sea ice classification. Remote Sens., 13(4), 552. doi.org/10.3390/rs13040552.

Lu, D., Liu, J., Shi, L., Zeng, T., Cheng, B., Wu, S., Wang, M., 2024. Retrieval of sea ice drift in the Fram Strait based on data from Chinese satellite HaiYang (HY-1D). Cryosphere, 18, 1419–1441. doi.org/10.5194/tc-18-1419-2024.

Meier, W.N., Stroeve, J., 2022. An updated assessment of the changing Arctic sea ice cover. Oceanography, 35(3–4), 10–19. doi.org/10.5670/oceanog.2022.114.

Muckenhuber, S., Korosov, A.A., Sandven, S., 2016. Open-source feature-tracking algorithm for sea ice drift retrieval from Sentinel-1 SAR imagery. Cryosphere, 10, 913–925. doi.org/10.5194/tc-10-913-2016.

Park, J.-W., Kim, H.-C., Korosov, A., Demchev, D., Zecchetto, S., Kim, S.H., Kwon, Y.-J., Han, H., Hyun, C.-U., 2021. Feasibility study on estimation of sea ice drift from KOMPSAT-5 and COSMO-SkyMed SAR images. Remote Sens., 13(20), 4038. doi.org/10.3390/rs13204038.

Park, J.-W., Kim, H.-C., Seo, M., Park, J.-E., Park, J., 2023. Sea ice drift tracking from SAR images and GPS tracker. Korean Journal of Remote Sensing, 39(3), 257–268. doi.org/10.7780/kjrs.2023.39.3.1.

Rabault, J., Müller, M., Voermans, J., Brazhnikov, D., Turnbull, I., Marchenko, A., Biuw, M., Nose, T., Waseda, T., Johansson, M., Breivik, Ø., Sutherland, G., Hole, L.R., Johnson, M., Jensen, A., Gundersen, O., Kristoffersen, Y., Babanin, A., Tedesco, P., Christensen, K.H., Kristiansen, M., Hope, G., Kodaira, T., de Aguiar, V., Mahoney, A.R., 2023. A dataset of direct observations of sea ice drift and waves in ice. Sci. Data, 10, 251. doi.org/10.1038/s41597-023-02196-2.

Sarlin, P.-E., DeTone, D., Malisiewicz, T., Rabinovich, A., 2020. SuperGlue: Learning feature matching with graph neural networks. Proc. IEEE/CVF Conf. Comput. Vis. Pattern Recognit. (CVPR), 4938–4947.

Scharien, R.K., Geldsetzer, T., Barber, D.G., Yackel, J.J., Langlois, A., 2010. Physical, dielectric, and C-band microwave scattering properties of first-year sea ice during advanced melt. J. Geophys. Res.: Oceans, 115(C12). doi.org/10.1029/2010JC006257.

Segal, R.A., Scharien, R.K., Cafarella, S., Tedstone, A., 2020. Characterizing winter landfast sea-ice surface roughness in the Canadian Arctic Archipelago using Sentinel-1 synthetic aperture radar and the Multi-angle Imaging SpectroRadiometer. Ann. Glaciol., 61(83), 284–298. doi.org/10.1017/aog.2020.48.

Shi, Q., Shi, F., Xu, R., Leppäranta, M., Zhai, X., Liu, J., 2024. Improved method for retrieving Arctic summer sea ice velocity based on FY-3D/MWRI brightness temperatures. Int. J. Digit. Earth, 17(1), 2420411. doi.org/10.1080/17538947.2024.2420411.

Spreen, G., Kwok, R., Menemenlis, D., 2011. Trends in Arctic sea ice drift and role of wind forcing: 1992–2009. Geophys. Res. Lett., 38(19). doi.org/10.1029/2011GL048970.

Sun, J., Shen, Z., Wang, Y., Bao, H., Zhou, X., 2021. LoFTR: Detector-free local feature matching with transformers. Proc. IEEE/CVF Conf. Comput. Vis. Pattern Recognit. (CVPR), 8922–8931.

Toole, J.M., Krishfield, R.A., Timmermans, M.-L., Proshutinsky, A., 2015. The Ice-Tethered Profiler: Argo of the Arctic. Oceanography, 24(3), 126–135. doi.org/10.5670/oceanog.2011.64.

Wang, X., Chen, Z., Fang, Y., Wang, R., Li, C., Li, G., 2023. An improvement in accuracy and spatial resolution of the pattern-matching sea ice drift from SAR imagery. Int. J. Digit. Earth, 16(2), 4073–4094. doi.org/10.1080/17538947.2023.2264918.

Zhang, M., An, J., Zhang, J., Yu, D., Wang, J., Lv, X., 2020. Enhanced Delaunay triangulation sea ice tracking algorithm with combining feature tracking and pattern matching. Remote Sens., 12(3), 581. doi.org/10.3390/rs12030581.

Zhao, L., Xie, T., Perrie, W., Yang, J., 2024. Sea ice detection from RADARSAT-2 quad-polarization SAR imagery based on co- and cross-polarization ratio. Remote Sens., 16(3), 515. doi.org/10.3390/rs16030515.